Pure & Appl. Chem., Vol.52, pp.1773-1800.
Pergamon Press Ltd. 1980. Printed in Great Britain.

0033-4545/80/0701-1773$02.00/0

ENERGY TRANSPORT IN THERMAL PLASMAS

E. Pfender

Heat Transfer Division, Dept. of Mechanical Engineering
University of Minnesota, Minneapolis, Minnesota 55455, USA

Abstract - This review is concerned with energy transport in current-carrying, thermal plasmas, in particular with energy transport close to and at the anode surface of high intensity arcs.

Experimental studies of the anode region of such arcs at atmospheric pressure reveal two types of anode arc roots which strongly affect the heat flux distribution. In relatively short arcs the action of the cathode jet leads to a diffuse anode attachment (cathode jet dominated mode). In contrast, simulations of long arcs clearly demonstrate a more or less severe constriction of the current path in front of the anode inducing an anode jet (anode jet dominated mode).

Modeling of the anode region under identical conditions confirms that the "natural" arc attachment in this situation will always be constricted, resulting in extremely high specific heat fluxes at the anode. The analysis also shows that enthalpy transport by the electrons is the dominating heat transfer mechanism in the anode region.

An analysis of the anode boundary layer of high current atmospheric pressure arcs indicates that presently available anode fall theories are not adequate for describing this zone. A one-dimensional analysis of the near-anode zone predicts negative anode falls in the range from one to three volts depending on the anode current density and on the plasma temperature. The electron temperature is substantially elevated over the temperature of the heavy particles close to the anode. Because of negative anode falls, the anode heat transfer model will no longer contain a term due to the anode fall. It is felt that this finding will be of great practical significance for the prediction of anode heat transfer in arc furnaces and in other applications which employ transferred arcs.

Calculations of the critical heat fluxes which lead to melting or evaporation of the anode surface in spite of intense water cooling of the rear face of the anode are in qualitative agreement with experimental findings.

1. INTRODUCTION

A gaseous plasma which consists in general of a mixture of electrons, ions and neutral particles may be produced from any gas or vapor in an electric discharge. Depending on the conditions in the discharge, two types of plasma may be observed, namely the "cold" or non-equilibrium plasma and the "hot" or equilibrium plasma. The latter, also known as a thermal plasma, is of particular interest in the context of this paper.

In contrast to "cold" plasmas which are characterized by high electron temperatures and low heavy particle temperatures, thermal plasmas can be described by a single temperature which is the same for all species in the plasma and which also governs excitations as well as chemical reactions in the plasma, i.e. a thermal plasma approaches a state of thermodynamic equilibrium or of Local Thermodynamic Equilibrium (LTE).

Thermal plasmas may be produced by high current electric arcs at atmospheric or higher pressures or in high frequency (rf) discharges under similar conditions. The ratio E/p (E = electric field strength, p = pressure) which is frequently used for distinguishing thermal plasmas from non-equilibrium plasmas assumes values around 10 V/m kPa in thermal plasmas and may exceed 10^4 V/m kPa in non-equilibrium plasmas.

In contrast to arc-produced thermal plasmas, rf plasmas are free from electrode contaminants

which is important for those applications requiring extremely clean plasma conditions.

Thermal plasmas found widespread applications for welding, for cutting and spraying, and for material melting as, for example, in arc furnaces. Since thermal plasmas are strong emitters of radiation ranging from the U.V. over the visible to the infrared part of the spectrum, they are widely used in the lighting industry.

Over the past years there seems to be an increasing awareness of the potential which thermal plasmas hold in the area of high temperature chemistry and material processing. Only a few selected examples will be mentioned which are characteristic of newer developments.

In the field of extractive metallurgy it has been demonstrated that iron oxides can be converted directly into pure molten iron in a single-step thermal plasma process using hydrogen and natural gas as reductants (1).

Plasma remelting and metal refining techniques are other areas which attract increasing interest. In refined steels as, for example, in chromium-nickel steels, nitrogen can be used as an efficient substitute for nickel. With a plasma remelting technique, 4-5 times more nitrogen can be incorporated into steel than with conventional methods resulting in a high tensile strength steel without nickel.

The production of ferro-alloys in plasma furnaces is another promising field. MacRae et al. (2) produced, for example, ferro-vanadium in a so-called falling-film plasma reactor using coal fines as a reductant.

By injection of particulate matter (usually fine powders) into arc-produced or rf thermal plasmas, the particles exposed to the hot plasma will melt and to a certain degree evaporate. Through the melting process the initially arbitrarily shaped particles will assume spherical shapes by contraction under the influence of surface tension. This process known as spheroidization is already a well-established industrial process (3,4).

Synthesis in thermal plasmas is of particular interest for making refractory materials of very high purity and with unusual properties. A typical example is the production of super conducting carbides in a plasma furnace (5). Another example is the production of solar-grade silicon using a thermal plasma reduction technique.

Coal gasification using arc processes is seriously considered as a possible option among other well-established coal gasification techniques.

Some of the previously mentioned and other applications are discussed in more detail in a number of surveys (6-11) which provide a representative cross section of present activities in high temperature plasma chemistry and material processing.

In general, thermal plasma processes resulting in high added-value materials will certainly have a great potential for industrial scale applications. In addition, those thermal plasma processes will be economically viable for which no alternate and simpler processing routes exist today.

Energy transport has been extensively studied from thermal plasmas to particulate matter injected into the plasma or to walls exposed to such plasmas (see for example (11,12)). Relatively little work has been done to clarify the energy transport in current-carrying plasmas, in particular in the electrode regions. Therefore, this survey will be devoted to the energy transport mechanisms in high current arcs with emphasis on the effects occurring in the anode region and on the anode itself. There is a twofold interest in these effects in connection with thermal processing. First of all the high intensity arc is the primary tool for producing thermal plasmas. Integrity and lifetime of the anode are of great concern in many arc plasma devices, because the anode is frequently subject to extremely high heat transfer rates. This is also true for the positive half-wave of a.c. arcs. Secondly, many thermal plasma processes utilize transferred arcs (arc furnaces, arc welding and cutting, etc.). In this situation it is desirable to maximize and shape the heat fluxes for optimizing the process.

The paper is divided into two parts. The first part deals with the anode region of high intensity arcs including modeling of the so-called anode contraction region and of the region immediately in front of the anode (anode boundary layer). The latter entails the development of a new anode fall theory which deviates substantially from previous work reported in the literature. Also included in this part are pertinent experiments performed in the author's laboratory. Most of this work has not yet been published.

In the second part, heat transfer to the anode will be reviewed including secondary effects on the anode (melting and evaporation).

2. THE ANODE REGION OF HIGH INTENSITY ARCS

In contrast to low intensity or low current arcs, high intensity arcs (I > 50 A) at atmospheric or higher pressures are characterized by strong macroscopic flows induced by the arc itself. Any variation of the current-carrying cross-section of the arc leads to induced flows (13). At sufficiently high currents and axial current density variations, flow velocities in the order of 100 m/s are observed. The cathode jet phenomenon in high intensity arcs is a typical example. In this case, the electron emission process at the cathode causes a contraction of the arc in front of the cathode which, in turn, gives rise to a continuous MHD pumping action producing the well-known cathode jet. A similar effect which may occur in the anode region of high intensity arcs will be discussed in a later part of this section.

The anode region of a high intensity arc may be divided into a flow-effected zone which is frequently identical with the anode contraction zone, a diffusion layer or anode boundary layer, and the sheath at the bottom of this boundary layer overlying the anode surface. Fig. 1 shows a sketch of these zones for a high intensity arc with constricted anode root. Also included in this sketch are typical dimensions of the various zones.

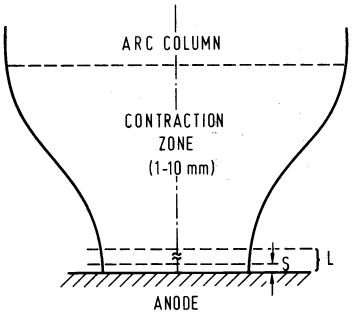

Fig 1 Schematic of the anode region of a high intensity arc with constricted arc root.
S = Sheath (~ λ_D Debye length)
L = Diffusion or boundary layer (~ 0.1 mm)

The flow-effected zone may show a substantial contraction of the current-carrying cross-section towards the anode as indicated in Fig. 1 or it may appear rather diffuse, revealing a characteristic bell shape.

These two different modes of anode arc attachment will be discussed in part 2.1 of this section.

The diffusion layer is characterized by strong axial gradients induced by the proximity of the low temperature anode. Therefore, this zone may also be classified as a boundary layer. Experiments in argon atmosphere reveal a relatively dark space in front of the anode which seems to be identical with this boundary layer. For an analysis of anode heat transfer, this zone plays a very important role which will be shown in part 2.3 of this section.

Finally, the sheath with a thickness in the order of a Debye length accomodates the transition from the gaseous plasma to the solid or liquid anode. Therefore, the sheath may be considered as an "electrical boundary layer." Within the sheath, substantial deviations from quasi-neutrality may occur which is associated with corresponding space charge induced electric fields (Poisson equation). The thickness of this sheath, however, is at least one order of magnitude smaller than the eletron mean free path. In fact, this thickness may be of the same order of magnitude as the roughness of an even polished anode (10^{-5} to 10^{-6} mm). For this reason the sheath is treated as a boundary condition in the analysis to be discussed in part 2.3 of this section.

2.1 EXPERIMENTAL STUDIES OF THE ANODE REGION

The size and shape of the anode arc attachment determines the magnitude and the distribution of local heat fluxes at the anode. Therefore, it is essential to determine the appearance of the anode arc root experimentally. In addition, those effects which exert a major influence on the anode arc root should be singled out.

The cathode jet experienced in high intensity arcs with velocities in the order of 100 m/s close to the cathode may have a strong effect on the anode region. In relatively short

arcs, the plasma assumes a characteristic bell shape caused by the cathode jet impinging on the anode surface (stagnation flow). An entirely different attachment is observed in the case of long arcs (arc length >> arc diameter) where the effect of the cathode jet is no longer felt at the anode. In this situation the arc shows a pronounced constriction in front of the anode.

Unfortunately, long arcs are inherently unstable. Therefore, an apparatus has been developed which allows us to simulate "long" as well as "short" arcs under identical and well stabilized conditions. The latter is a prerequisite for basic studies of the anode region of such arcs (14). The desired unobstructed viewing of the anode region suggests a plane anode geometry with the arc axis normal to the anode surface. This geometry finds use in many arc applications and it also lends itself to modeling.

2.1.1 ARC ARRANGEMENT

Fig. 2 shows a schematic diagram of the arc configuration. The arc is operated between a thoriated tungsten cathode and a plane water cooled anode which is perpendicular to the axis of the rotationally symmetric arc. Stability of the arc column and rotational symmetry are ensured by a segmented water cooled constrictor tube with an inside diameter of 10 mm. In contrast to conventional constrictor tubes the segments in this design are separated by a distance of 1 mm from each other in order to reduce the pressure gradient along the tube. This provision is crucial for simulating long arcs in which flow effects from the cathode must be substantially reduced in the vicinity of the anode. The total length of the arc is approximately 120 mm, i.e. the arc length exceeds its diameter by more than one order of magnitude.

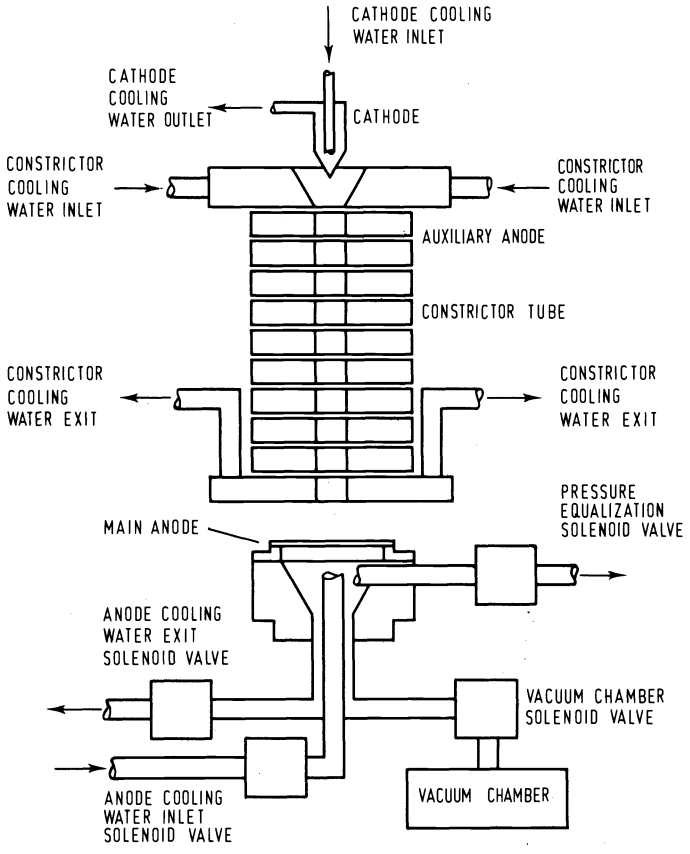

Fig 2 Schematic diagram of the arc configuration.

The arc is initiated between the cathode and the auxiliary anode located on top of the constrictor tube. The cathode jet provides sufficient ionization within the constrictor tube so that the arc can be transferred to the main anode.

The anode consists of a flat Cu disk 44 mm in diameter. This relatively large diameter eliminates any artificial reduction of the size of the anode arc root. An external motor drive allows us to vary the gap between the last segment of the constrictor tube and the anode surface.

In many high current arc applications melting and evaporation of anode material is either inevitable or even desirable. For a study of the effects of anode melting and evaporation on the behavior of the anode arc root, a controlled overheating of the anode is provided. Valves in the cooling water supply and outlet lines to the anode can be shut off at the start of the experiment (Fig. 2). After a controlled time interval, another valve makes a connection to an evacuated container which removes the remaining water from the anode cooling chamber. Finally, an additional valve connected to the gas atmosphere in the discharge chamber equalizes the pressure between the front and rear face of the anode. The timing and sequencing of the valves is controlled by a microprocessor.

The previously described electrode arrangement is mounted in a large discharge chamber (Fig. 3) which allows control of the gas atmosphere. Viewing ports in this chamber permit the observation of the anode region of the arc from different directions.

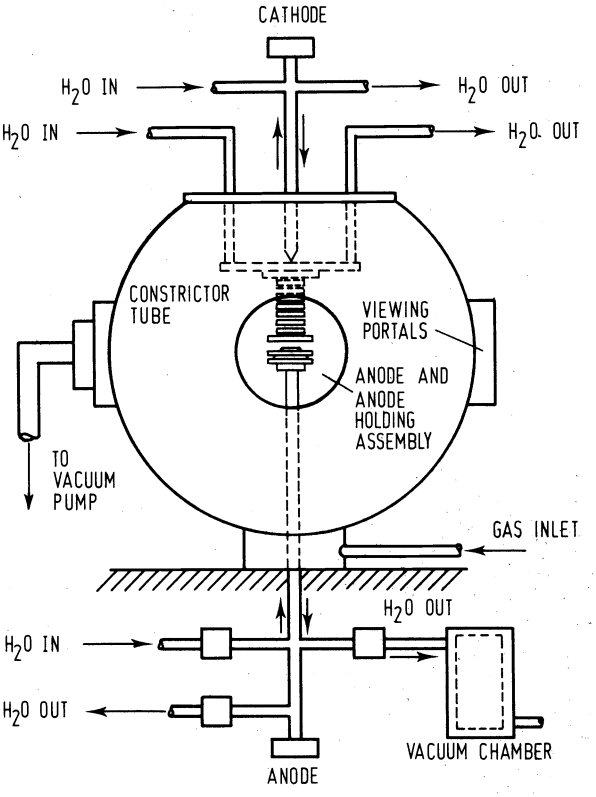

Fig 3 Discharge chamber with arc arrangement.

For the transient experiments, a high speed Fastax camera is used for photographing the sequence of events in the anode region. The camera as well as the timing marks on the film are also controlled by the previously mentioned microprocessor. In addition, a monochromator is employed for detecting the appearance of Cu vapor in the anode region. The arrangement for this measurement is shown in Fig. 4.

A mirror-scanning arrangement allows horizontal and vertical positioning of the source on the slit of the monochromator. The radiation intensity is measured with a photomultiplier,

amplified and recorded on a strip chart recorder. The region immediately in front of the anode surface is focused on the entrance slit of the monochromator which is adjusted to a wave length of 5218.2 Å (strong Cu line). Details of the experimental procedure are described in Ref. (14). The most important results of these studies will be discussed in the following paragraph.

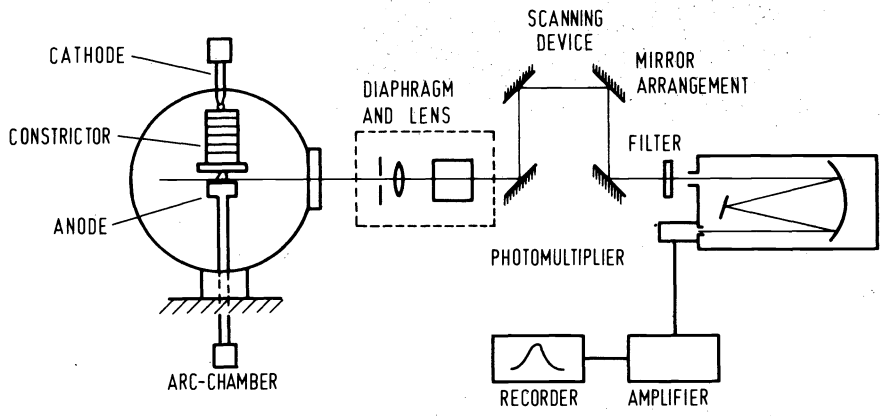

Fig 4 Optical arrangement for detecting anode vapor.

2.1.2 RESULTS

The results presented in this paragraph refer to arcs operated in argon at 1 atm (≈ 100 kPa) and currents between 100 and 300 A. Since the arc is enclosed in a constrictor tube, its characteristic is rising over the entire current range. Both sharp and rounded cathode tips are utilized in these experiments. The shape of the cathode tip has a pronounced effect on the velocity of the self-induced flow. With a sharp tip, velocities in excess of 600 m/s have been measured at a distance of approximately 1 mm from the cathode in an atmospheric pressure, free-burning argon arc at 200 A (15).

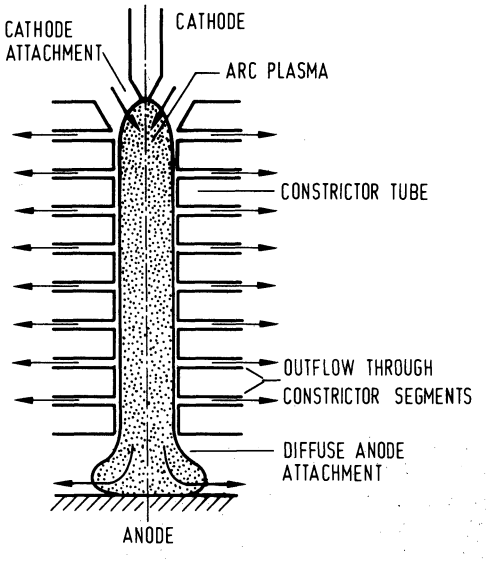

Fig 5 Schematic of the Cathode Jet Dominated (CJD) mode of anode arc attachment.

Deterioration of the cathode tip as a natural consequence of arc operation may reduce the velocity by 50%. Therefore, by rounding of the cathode tip, the flow induced at the cathode can be controlled within certain limits. Another possibility of cathode flow control is provided by the design of the constrictor tube (gaps between segments). Although the application of both controlling mechanisms reduces the effect of the cathode flow in the anode region substantially, this cathode flow cannot be entirely eliminated.

In general, a sharp-tipped cathode in conjunction with high current levels (I > 150A) produces in this arc arrangement a diffuse anode attachment as indicatd schematically in Fig. 5. Some of the flow induced at the cathode impinges on the anode surface producing the well-known flow pattern of short high intensity arcs. Since the cathode jet is responsible for this mode of anode arc attachment, it will be denoted as "Cathode Jet Dominated" (CJD). Fig. 6 shows a photograph of this mode. As the current increases, the stagnation region becomes more pronounced because the maximum cathode jet velocity increases with current according to the relationship (16)

$$v_{max} \sim (jI)^{1/2}$$

where j is the current density at the cathode and I the total current. Fig. 6 also indicates a thin, relative dark space in front of the anode which will be discussed in part 2.3 of this section.

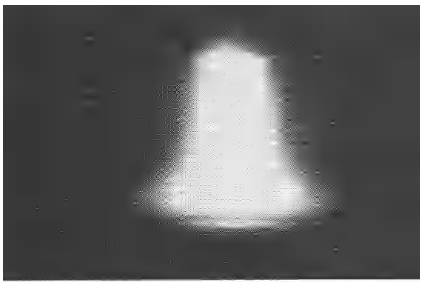

Fig 6 Photograph of the CJD mode.

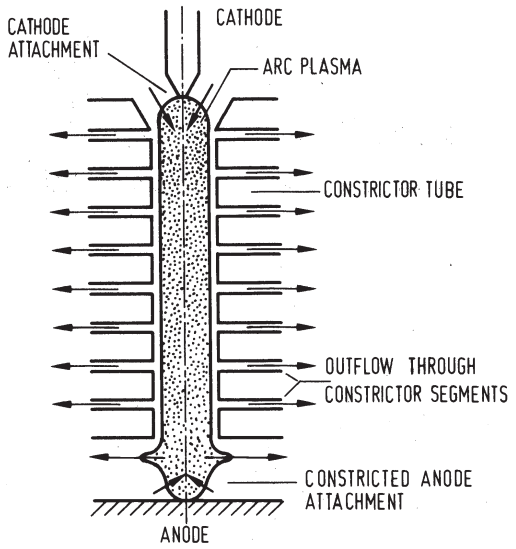

Fig 7 Schematic of the Anode Jet Dominated (AJD) mode of anode arc attachment.

At lower current levels (I < 150A) and with a rounded cathode tip an entirely different mode of anode arc attachment is observed displaying a more or less severe constriction of the arc channel in front of the anode. This constriction, in turn, induces an anode jet. Therefore, this mode of attachment will be denoted as "Anode Jet Dominated" (AJD). Fig. 7 shows a schematic diagram and Fig. 8 a photograph of this mode. Since there is still some flow from the cathode jet approaching the anode, the flow induced at the anode impinges with the cathode flow forming a stagnation layer which is clearly visible in Fig. 8.

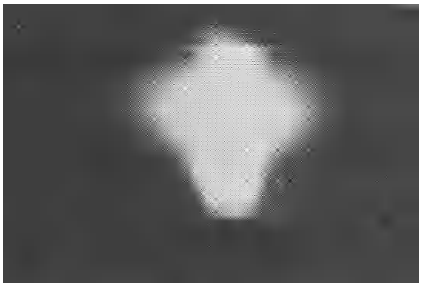

Fig 8 Photograph of the AJD mode.

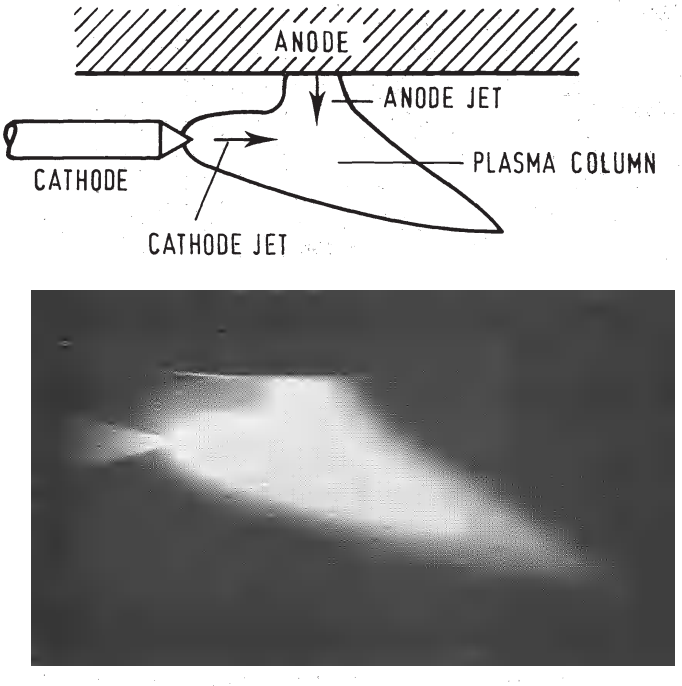

Fig 9 Interaction of cathode and anode jet in a high intensity arc.

Although low current levels and a rounded cathode tip encourage the AJD attachment, this mode may also be obtained at higher current levels and with a sharp cathode tip, provided that other means can be found to reduce the effect of the cathode flow at the anode. Increasing the gap d between the last segment and the anode surface is, for example, a very effective means to produce the AJD attachment. After the AJD mode has been established, the arc current may be increased within certain limits or d decreased without returning to the CJD mode. The transition from the AJD to the CJD mode depends on the relative strength of cathode and anode jets.

These findings clearly demonstrate that in the case of long arcs or negligible cathode flow effects at the anode, the arc attachment at the anode will be constricted (AJD). Therefore, this mode of attachment may be considered as the "natural" anode arc attachment if secondary effects from the cathode are excluded. Fig. 9 shows a typical example of this "natural" anode arc attachment. With the cathode parallel to the anode surface, the

cathode jet will no longer impinge on the anode and, therefore, the arc column constricts in front of the anode producing an anode jet. The relative strengths of cathode and anode jets determine the angle of deflection of the plasma flame. A model developed for the AJD mode will be discussed in part 2.2 of this section.

Considering the effects of melting and evaporation of the anode on the anode region, no final conclusions can be drawn. Experiments at different current levels reveal a transition from the CJD to the AJD mode as Cu vapor enters the arc plasma. In some cases, however, the AJD mode reverts back to the CJD mode. Contrary to expectations "seeding" of the arc with Cu vapor does not increase the arc diameter and lower the arc resistance although Cu with an ionization potential of 7.7 V should be readily ionized at the lower temperature levels in the arc fringes. It may be speculated that the energy extraction (heating and ionization of the vapor, radiation losses) caused by the anode vapor entering the arc plasma overbalances the seeding effect.

2.2 MODELING OF THE ANODE CONTRACTION ZONE

In spite of extensive research efforts over the past 30 years, there is still a lack of basic understanding of the anode region of high intensity arcs. The complexity of this region, caused by the interaction of electric, magnetic, thermal and fluid-dynamic effects does not easily lend itself to a theoretical treatment. Therefore, it is not surprising that there is still no comprehensive theory which would describe all the observed phenomena in this region.

The model which has been adopted for describing this region takes an initial constriction of the arc adjacent to the anode into account. This initial constriction is a consequence of the low temperature of the anode and the associated heat conduction losses from the arc to the anode. Since the current density j as well as the self-magnetic field B (strictly speaking the magnetic induction) increase towards the anode, the magnetic pinch effect leads to an entrainment of cold gas (radial flow) into the anode region. This entrainment causes a severe cooling of the arc fringes resulting in a corresponding reduction of the arc diameter. As the arc constricts, the pumping action due to the $\vec{j} \times \vec{B}$ interaction is enhanced, causing an even more severe constriction. This seemingly unstable constriction mechanism is balanced by the increasing temperature gradient which tends to expand the arc by heat conduction. Based on this model, the conservation equations for the anode region of a rotationally symmetric arc are solved numerically with appropriate boundary conditions.

In contrast to previous studies (17, 18) which considered essentially the same problem, a more sophisticated numerical technique is employed which also eliminates the need for some artificial assumptions and boundary conditions for the solution of the momentum equation. In addition, an important term is introduced into the energy equation which describes the enthalpy transport by the electron current. This term also provides a "natural" boundary condition at the sheath edge (interface between contraction zone and anode fall zone) eliminating the previously required (17, 18) assumption of temperature gradients which match the order of magnitude of observed anode heat fluxes. As the results of this study demonstrate, enthalpy transport by the electron current is the dominating axial energy transport mechanism in the anode region. Therefore, axial heat conduction across the sheath edge will be neglected in the present model. Although this approach appears reasonable as far as the energy balance is concerned, the relatively small axial conduction term may have a significant influence on the shape of the isotherms close to the sheath edge. In a later, more advanced model this effect will be taken into account.

2.2.1. ANALYTICAL MODEL

The model adopted for this analysis is based on a rotationally symmetric arc with the main body of the arc column enclosed by a constrictor tube so that the arc column may be considered as fully developed. This fact will be used for formulating the boundary conditions at the interface between arc column and contraction zone. A sketch of the contraction zone is shown in Fig. 1 which also indicates approximate dimensions of the entire anode region.

Since the anode in a high intensity arc has to sustain very high heat fluxes, integrity of the anode is ensured by an efficient cooling system. Near the anode surface, the surrounding gas will also assume a relatively low temperature. Since gases below a certain critical temperature will not conduct electric current, cooling of the arc fringes near the anode results in a reduction of the arc cross section (thermal pinch). This initial contraction gives rise to the entrainment of cold gas via the magnetic pinch effect which is finally stabilized by increasing heat conduction in radial direction.

BASIC ASSUMPTIONS AND GOVERNING EQUATIONS

throughout this analysis the following assumptions will be used:

a) The arc is steady and rotationally symmetric.
b) Local Thermodynamic Equilibrium (LTE) prevails over the entire contraction zone and the plasma is treated as a perfect and optically thin gas
c) Thermal diffusion effects are neglected.
d) Gravity and viscous heat dissipation are negligible.
e) Flow velocities are substantially less than the velocity of sound ($M < 1$).

Based on these assumptions the conservation equations are expressed in terms of cylinder coordinates (r, x, θ), where r is the radial distance, x the axial distance and θ the angle.

mass:
$$\frac{\partial}{\partial x}(\rho u) + \frac{1}{r}\frac{\partial}{\partial r}(\rho r v) = 0 \tag{1}$$

$$\rho u \frac{\partial u}{\partial x} + \rho v \frac{\partial u}{\partial r} = -\frac{\partial p}{\partial x} + 2\frac{\partial}{\partial x}\left(\mu \frac{\partial u}{\partial x}\right) \tag{2}$$

$$+ \frac{1}{r}\frac{\partial}{\partial r}\left(\mu r \frac{\partial u}{\partial r}\right) + \frac{1}{r}\frac{\partial}{\partial r}\left(\mu r \frac{\partial v}{\partial x}\right) + j_r B_\theta$$

momentum:
$$\rho u \frac{\partial v}{\partial x} + \rho v \frac{\partial v}{\partial r} = -\frac{\partial p}{\partial r} + \frac{\partial}{\partial x}\left(\mu \frac{\partial v}{\partial x}\right) + \frac{2}{r}\frac{\partial}{\partial r}\left(\mu r \frac{\partial v}{\partial r}\right) \tag{3}$$

$$+ \frac{\partial}{\partial x}\left(\mu \frac{\partial u}{\partial r}\right) - \frac{2\mu v}{r^2} - j_x B_\theta$$

Since $j_x \gg j_r$, the self-induced magnetic field has only a B_θ component which may be written

$$B_\theta = \frac{\mu_o}{r}\int_o^r j_x \xi d\xi \tag{4}$$

Current continuity requires that

$$\frac{\partial j_x}{\partial x} + \frac{1}{r}\frac{\partial}{\partial r}(r j_r) = 0 \tag{5}$$

Finally, the energy conservation equation takes the form

$$\rho c_p u \frac{\partial T}{\partial x} + \rho c_p v \frac{\partial T}{\partial r} = \frac{5}{2}\frac{k_B}{e}\left(j_x \frac{\partial T}{\partial x} + j_r \frac{\partial T}{\partial r}\right)$$

$$+ \frac{\partial}{\partial x}\left(k \frac{\partial T}{\partial x}\right) + \frac{1}{r}\frac{\partial}{\partial r}\left(kr \frac{\partial T}{\partial r}\right)$$

$$+ \frac{(j_x^2 + j_r^2)}{\sigma} - S_R \tag{6}$$

In addition, Ohm's law is used in integrated form

$$I = 2\pi \int_0^r j_x \xi d\xi \qquad \text{with } j_x = \sigma E_x \tag{7}$$

In these equations, ρ, u, v, p, μ, j, and B represent the plasma density, the axial velocity, the radial velocity, the pressure, the viscosity, the current density, and the magnetic field, respectively. The indices x, r, and θ indicate the corresponding directions in cylinder coordinates. In Eq. (4) μ_o represents the permeability of vacuum and ξ a dummy variable. In the energy equation (Eq. (6)) the symbols c_p, T, k_B, e, k, σ and S_R are, respectively, the specific heat at constant pressure, the absolute temperature, the Boltzmann constant, the elementary charge, the thermal conductivity, the electrical conductivity, and the optically thin radiation emitted per unit volume. I is the total current in the arc.

The left hand side of Eq. (6) represents the convection term. The first term on the right hand side stands for the electron enthalpy flux, which is the energy transported by the electrons traveling towards the anode. In vector notation this term may be expressed by $\vec{j}\cdot$grad T. This term vanishes in a fully developed arc column because $\vec{j}$ and grad T are normal to each other. In the contraction zone, however, $\vec{j}\cdot$grad T cannot be neglected; in fact it may be the dominating term as far as axial heat transport is concerned.

By specifying appropriate boundary conditions for the field variables u, v, p, T, I, and j, the conservation equations can be solved provided that thermodynamic and transport properties (ρ, c_p, μ, k, σ, and S_R) are known. Under the assumption of LTE, these properties are only functions of the temperature. Details of the boundary conditions, the transport coefficients and the solution method are described in Refs. (19, 20).

2.2.2. RESULTS

The isotherms (solid lines) and flow lines (dashed lines) for an arc in nitrogen and argon atmosphere are shown in Figs. 10 and 11 as typical examples. Since the electrical conductivity of gases below a certain critical temperature (6000 K for atmospheric pressure argon and nitrogen) becomes negligible small, the arc periphery is defined as this particular isotherm. It is seen that the arc periphery (indicated by the heavy line) moves inward as

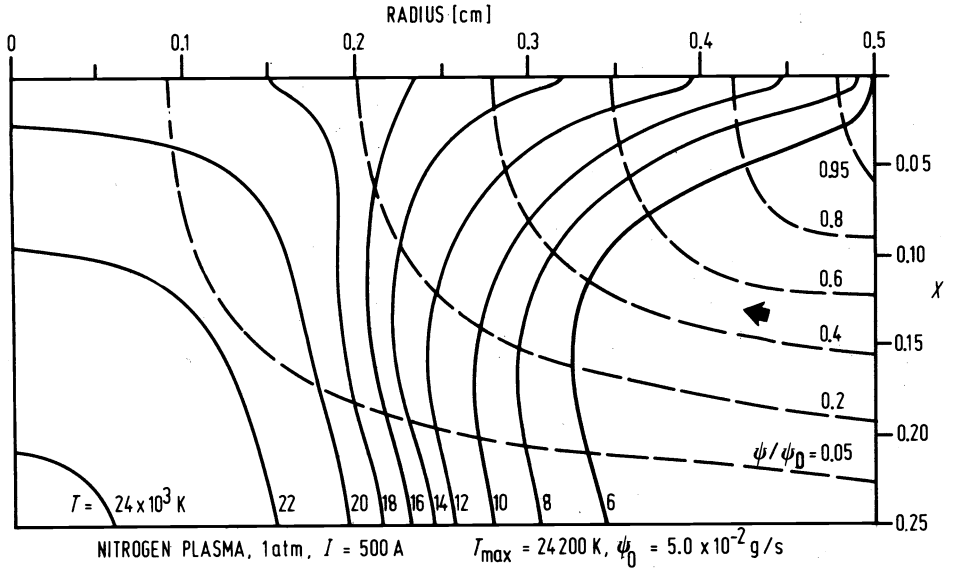

Fig 10 Isotherms and streamlines in the anode region of a nitrogen arc. (p = 1 atm, I = 500 A, T_{max} = 24,200 K, ψ_o = 5 x 10^{-5} kg/s).

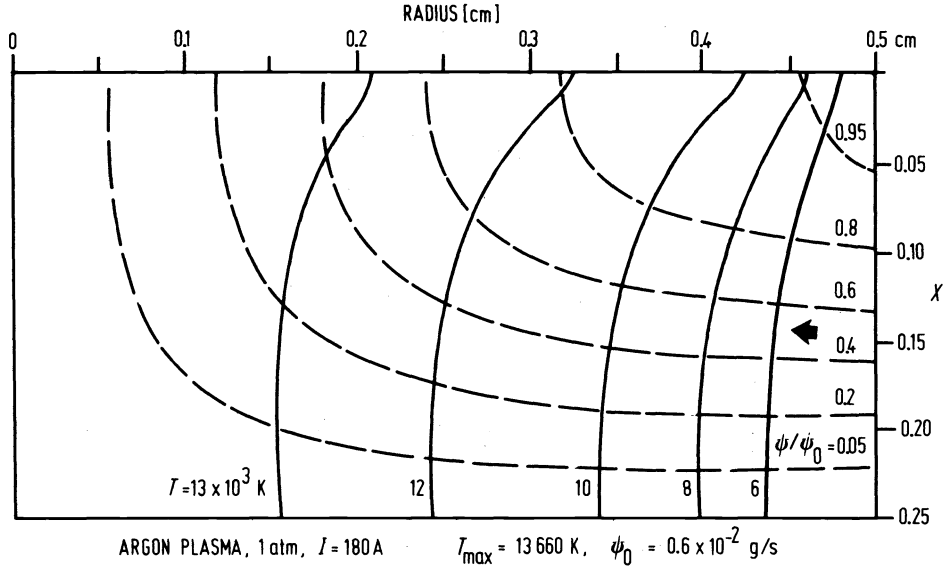

Fig 11 Isotherms and streamlines in the anode region of an argon arc. (p = 1 atm, I = 180 A, T_{max} = 13,660 K, ψ_o = 0.6 x 10^{-5} kg/s).

the anode is approached. The reduction in arc diameter is rather severe for nitrogen arcs at higher current levels (Fig. 10). The flow (indicated by arrows) is primarily responsible for the cooling effect imposed on the arc and, therefore, it has a strong effect on the temperature distribution. The maximum axial velocity is found near the center line (up to 200 m/s). This value is compatible with measurements of flow velocities in free burning arcs induced by the cathode jet (15). The maximum temperature near the sheath edge is in this case 24,200 K -- a substantial increase from the temperature at the column end (18,500 K). The situation is markedly different in argon arcs at lower current levels as shown in Fig. 11. Since the arc contraction is relatively small, the center line temperature increases only slightly. This difference may be attributed to the magnitude of the flow (anode jet) which is substantially higher in the previous case (Fig. 10). Other factors, such as the plasma properties, which also affect the behavior of the arc, will be discussed later in this section.

The results also show that the flow penetrates deeper into the arc for lower currents. The fact that the flow at higher current levels is forced to turn around earlier than in the case of lower current levels seems to be contradictory because in the case of higher currents a stronger Lorentz force is induced to drive the flow. According to the momentum equation part of the driving force $\vec{j} \times \vec{B}$ is used for accelerating the flow, part for building up a pressure gradient, and part is lost by friction. Because of the higher temperatures in the arc core at higher current levels, the plasma density decreases accordingly and, at the same time, the viscosity increases. Lower plasma density and higher viscosity reduce the amount of gas which is able to enter the core region, i.e. the arc core approaches the behavior of a solid body as far as the flow is concerned. This effect manifests itself by a larger radial pressure gradient $\partial p/\partial r$ which forces the flow to turn in axial direction.

As mentioned before, the flow field is induced by the radial component of the Lorentz force $j_x B_\theta$ which, in turn, has its origin in the axial current flux j_x. In order to understand why arcs at different current levels behave differently, the j_x distributions for the previous two cases are plotted in Figures 12 and 13. For the lower current (180 A) arc, the axial current density distribution j_x in Fig. 12 is as expected. The peak values always occur on the center line (r = 0) and they increase with decreasing distance from the anode. The increase of these peak values of j_x from the column (x/x_o = 0) towards the anode (x/x_o = 1) is obviously a consequence of arc contraction. Notice that the peak value

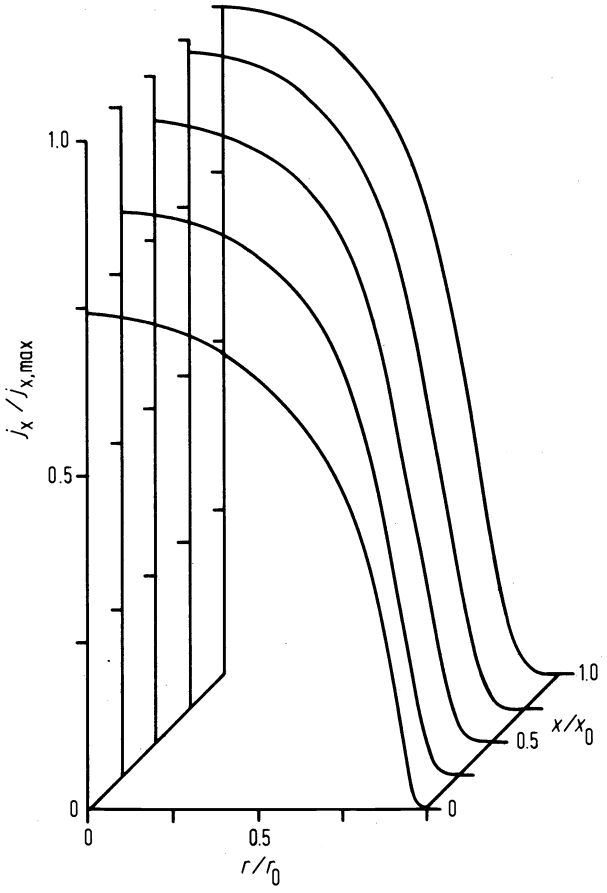

Fig 12 Normalized axial current density distribution $j_x(r)$ in the anode region of an argon arc. (p = 1 atm, I = 180 A, $j_{max} = 5.08 \times 10^6$ A/m^2, $\psi_o = 0.6 \times 10^{-5}$ kg/s).

of j_x at the anode end is only 25% higher than that of the column, which indicates a mild contraction.

For nitrogen arcs at higher currents (500 A), however, this difference is more pronounced. In Fig. 13, the ratio of peak values of j_x at the anode end and the column is approximately 3 to 1. This is due to the more severe contraction at higher current levels. Compared with the previous case, the current density profiles in the contraction zone are rather flat in the center part, rising gradually towards the fringes and forming an off-axis peak near $r/r_o = 0.5$. At this location, axial convection, q_u, shows also a maximum as indicated in Fig. 14.

The arc responds to this enhanced convective energy loss by an increase in field strength which seems to overcompensate the lower electrical conductivity at this location leading to a slight off-axis current density peak.

The various heat transfer mechanisms as described by the energy equation (Eq. 6) determine the temperature field. There are three fluxes that transport energy across a given control volume surface: the convective heat flux $\vec{q}_v = \rho c_p \vec{v} T$, the conductive heat flux $\vec{q}_k = -k\nabla T$ and the electron enthalpy flux $\vec{q}_j = -\frac{5}{2}\frac{k_B}{e}\vec{j}\,T$. In addition, there are two source terms: the Joulean dissipation j^2/σ and the radiative loss $-S_R$. Since the energy exchange

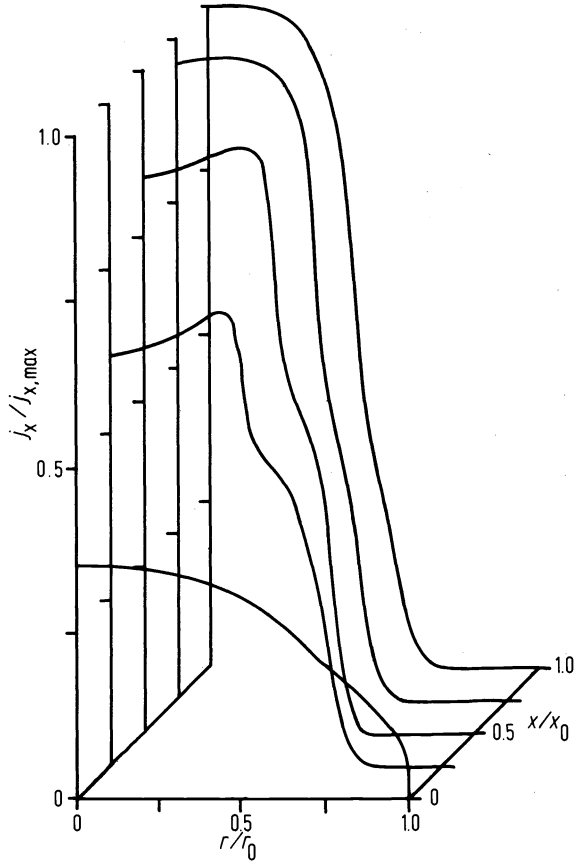

Fig 13 Normalized axial current density distribution $j_x(r)$ in the anode region of a nitrogen arc. (p = 1 atm, I = 500 A, $j_{max} = 2.8 \times 10^7$ A/m^2, $\psi_o = 5 \times 10^{-5}$ kg/s).

processes for high current arcs are more pronounced, a 500 A nitrogen arc will be considered as a representative example.

The right hand side of Fig. 14 shows the variations of the fluxes q_u, q_{j_x}, and q_{k_x} across a surface A-A in the middle of the contraction zone ($x/x_o = 0.5$). Since q_{j_x} is related to the current density j_x (see Fig. 13), the center part of this curve is rather flat due to the slight off-axis peak of the current density. The positive value of q_{j_x} indicates that its direction is towards the anode. The convection q_u is of approximately the same order of magnitude but with the opposite sign, indicating that convection is directed towards the arc column. The rather sudden variations of the q_u distribution follow essentially the variation of the specific heat. Both of them show peaks around 7,000 K and 15,000 K. The axial conduction term q_{k_x} is approximately one order of magnitude smaller than the other two terms. Near the center part of the arc, the negative q_{k_x} indicates that the temperature is increasing towards the anode, while the positive q_{k_x} near the fringes implies an opposite temperature gradient in that region. The variation of q_{k_x} correlates well with that of the thermal conductivity k. The left part of Fig. 14 provides similar information for the surface B-B near the anode ($x/x_o = 0.9$). The value of q_{j_x} is approximately 30%

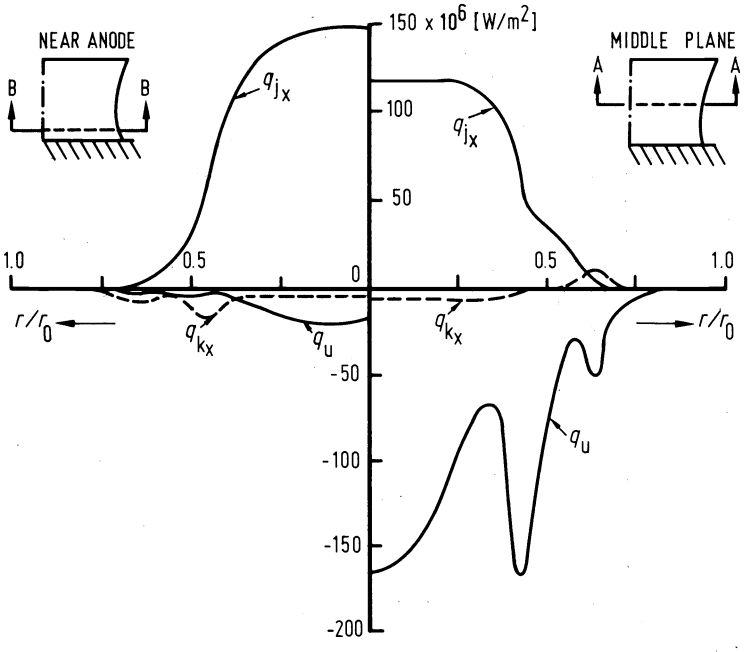

Fig 14 Axial heat fluxes in the near anode and midplane section of the anode contraction zone of a nitrogen arc. (p = 1 atm, I = 500 A, ψ_o = 5 x 10^{-5} kg/s; q_{k_x} = conduction, q_u = convection, q_{j_x} = enthalpy transport by the electron current).

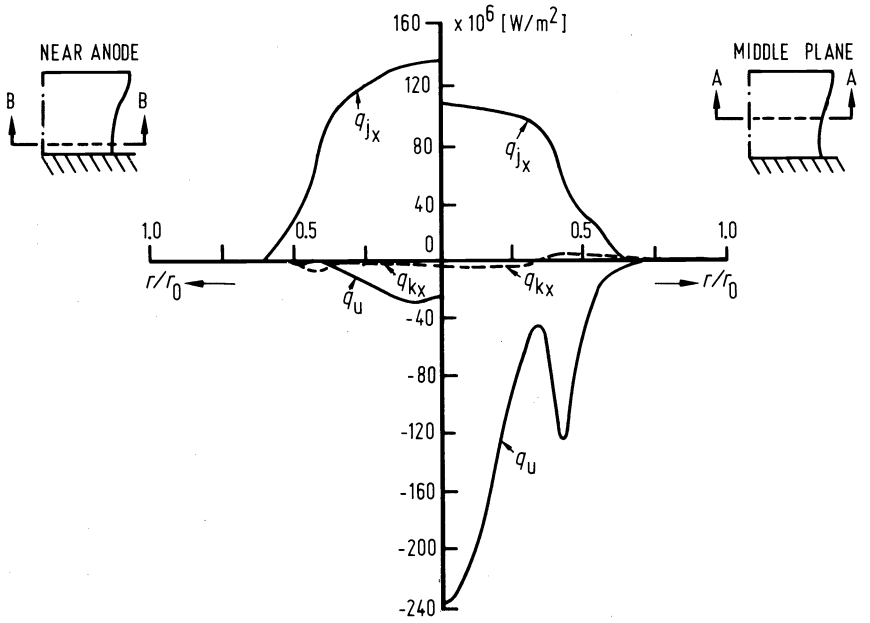

Fig 15 Axial heat fluxes in the near anode and midplane section of the anode contraction zone of an argon arc. (p = 1 atm, I = 500 A, ψ_o = 6.3 x 10^{-5} kg/s).

larger than that experienced at surface A-A. This increase results from both the larger current flux j_x and the higher local temperature T. Although the shape of the profile of q_u remains almost the same, its magnitude is drastically reduced in this case. The conduction q_{k_x} is even smaller. It is obvious that the heat flux term q_{j_x} is by far dominating across surface B-B. This fact justifies our earlier assumption that axial conduction at the anode end of the contraction region is negligible ($x/x_o = 1$) in comparison to enthalpy transport by the electron current.

A similar set of curves is shown for an argon arc at 500 A in Fig. 15. In general, the trend of the various mechanisms is the same although there are minor differences due to different plasma properties. Experimental evidence indicates that argon arcs are generally less constricted in the anode region than nitrogen arcs. This phenomenon will be explained briefly in the following. The reasoning again hinges on the differences of the plasma properties for these two gases. A comparison of corresponding values reveals that nitrogen plasmas have a much higher specific heat than argon plasmas at the same temperature. Also, there is an additional peak in c_p for nitrogen between 6,000 and 8,000 K (dissociation of the N_2 molecule). As shown earlier, convective heat transfer is very effective in the middle of the contraction zone, where contraction is most likely to occur. Since the convection process is influenced by both the mass flux $\rho\vec{v}$ and the specific heat c_p, it is easy to see why nitrogen arcs are more sensitive to the fringe cooling effect than argon arcs for the same total mass flow rate. And hence, the contraction of argon arcs is not as severe as for nitrogen arcs under similar operating conditions.

Although one may conclude from Figures 14 and 15 that the dominating axial heat fluxes at the mid-plane of the contraction zone are q_j and q_u, while the only important heat flux near the end of the contraction zone is q_j, the balance of these fluxes together with the two energy source terms shows a completely different picture. In order to compare the energy gained or lost by each individual mechanism, the following integrals are defined for a single control volume ΔV:

$$\varepsilon_{\vec{v}} = -2\pi\Delta x \int_o^r \rho\, c_p \vec{v} \cdot \text{grad } T\, r\,dr$$

$$\varepsilon_{\vec{j}} = 2\pi\Delta x \int_o^r \frac{5}{2}\frac{k_B}{e}\vec{j} \cdot \text{grad } T\, r\,dr$$

$$\varepsilon_k = 2\pi\Delta x \int_o^r \text{div } (k \text{ grad } T)\, r\,dr$$

$$\varepsilon_\sigma = 2\pi\Delta x \int_o^r \frac{j^2}{\sigma}\, r\,dr$$

$$\varepsilon_R = -2\pi\Delta x \int_o^r S_R\, r\,dr$$

The various ε's represent the energy generated or lost per unit time in the defined control volume and they should sum up to zero for a steady-state arc. These energy quantities can then be compared for control volumes at different locations. In Fig. 16, the radial variation of the ε's are plotted for control volumes in the midplane of the contraction zone ($x/x_o = 0.475$) for a nitrogen arc at 500 A. The ε_σ is the major energy source inside the arc. It first increases almost linearly with respect to the radius r due to the increase of control volume size, and finally tapers off as the current flux j drops sharply near the arc periphery. Compared with ε_σ the radiative loss ε_R is rather small, which is consistent with earlier findings. The net energy gain or loss due to the electron enthalpy flux, denoted by ε_j, is rather small, which does not contradict the results shown in Fig. 14. Although q_{j_x} carries a large amount of energy into a C.V., a similar amount of energy is leaving the same C.V. through the opposite surface in the same direction. Consequently the net energy transport ε_j, into or out of the control volume is rather small.

The two most important energy transport mechanisms in Fig. 16 as far as net transport of energy into or out of the control volume is concerned are convection $\varepsilon_{\vec{v}}$ and conduction ε_k.

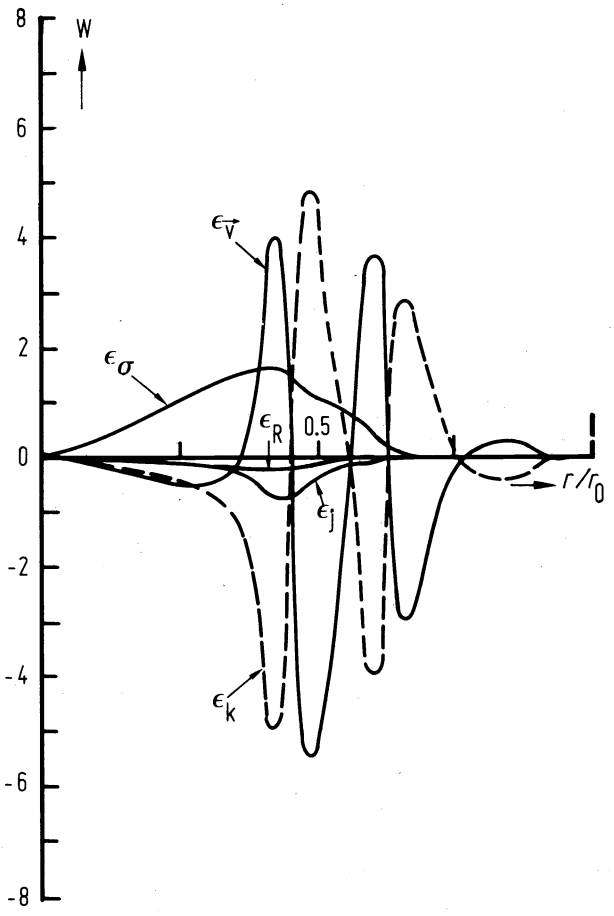

Fig 16 Energy exchange in a midplane control volume of the anode contraction zone of a nitrogen arc. (p = 1 atm, I = 500 A, $\psi_o = 5 \times 10^{-5}$ kg/s; ϵ_σ = heat dissipation, ϵ_k = conduction, $\epsilon_{\vec{v}}$ = convection, ϵ_j = enthalpy transport by the electron current, ϵ_R = radiation).

Except near the center part of the arc, these two contributions seem to almost cancel each other. The fact that ϵ_k is important for this consideration does not contradict the earlier result that axial conduction q_{k_x} is small (Fig. 14). It rather reflects the fact that conduction in radial direction q_{k_r} plays an important role in the energy balance. The large amplitudes and the sign variation of $\epsilon_{\vec{v}}$ and ϵ_k indicate the complexity of the plasma heat transfer process. For a detailed interpretation of these curves, the temperature as well as the flow fields have to be taken into account in conjunction with the variation of the transport properties.

In Fig. 17, similar ϵ profiles are presented for control volumes located near the anode end (x/x_o = 0.875). Basically, these two figures provide the same type of information with minor differences. The amount of energy exchanged between $\epsilon_{\vec{v}}$ and ϵ_k is larger in the fringes than that in the center according to Fig. 16, whereas Fig. 17 shows a shift of this energy exchange towards the arc center ($\frac{r}{r_o} = 0.5$).

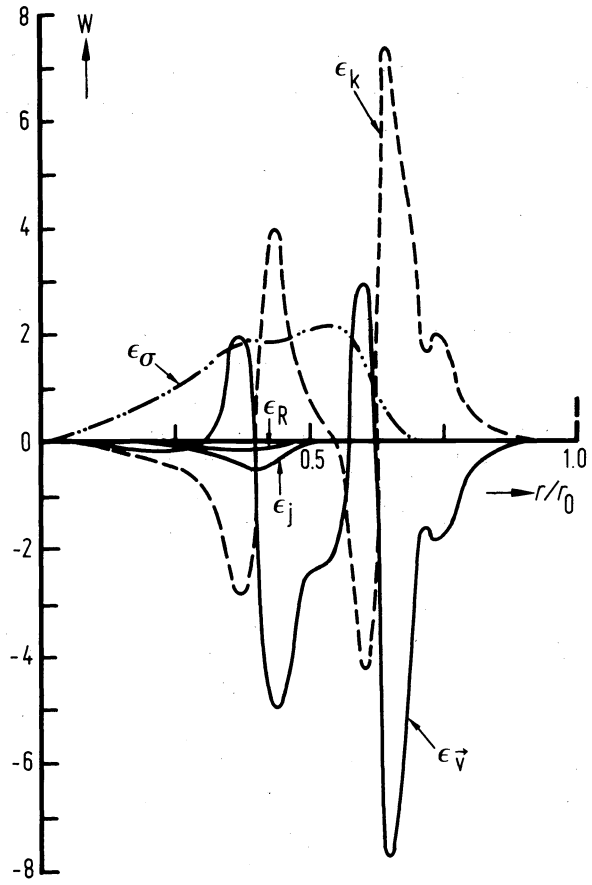

Fig 17 Energy exchange in a near anode control volume of the anode contraction zone of a nitrogen arc. (p = 1 atm, I = 500 A, $\psi_o = 5 \times 10^{-5}$ kg/s; ϵ_σ = heat dissipation, ϵ_k = conduction, ϵ_v = convection, ϵ_j = enthalpy transport by the electron current, ϵ_R = radiation).

2.3 MODELING OF THE ANODE BOUNDARY LAYER

The anode diffusion or anode boundary layer is defined as the zone in front of the anode which is affected by the presence of the low temperature anode. For the situation considered in this paper, this layer has a thickness in the order of 0.1 mm which is substantially larger than the mean free path length of the electrons. Therefore, this layer may be treated as a continuum.

The steep gradients of temperature and particle densities in this zone give rise to diffusional fluxes which must be considered in the governing equations. The heavy particle temperature, for example, drops in this zone from the plasma temperature to typical anode temperatures ($\leq$ 1000 K). If LTE would prevail throughout this zone, the electrical conductivity would be almost zero in front of the anode, violating the requirement of current continuity. This implies that the electron temperature must be substantially higher than the heavy particle temperature, i.e. there will be appreciable deviations from LTE within the anode boundary layer.

As previously mentioned, there is another layer located at the bottom of the anode boundary layer overlying the anode surface, known as the sheath. The thickness of this sheath is several orders of magnitude less than the thickness of the anode boundary layer. In general, the anode fall is identified with the potential drop across the sheath because within the sheath there are strong electric fields due to deviations from quasi-neutrality. Considering the problems associated with measurements of potential drops over the thickness of the sheath, it appears more useful to consider the potential drop over the entire anode boundary layer as the anode fall. This approach has been adopted for the following

considerations because most of the potential drop is within the sheath. The error involved in this approach is small.

The principal task of the anode fall, namely to provide an electrical connection between the high temperature plasma of the arc and the low temperature anode embraces several effects imposed by the conservation equations. Conservation of energy requires, for example, that field strength and current density adjust themselves so that the total net energy losses suffered by a volume element are compensated for by the ohmic heating in the same volume element. Because of the steep gradients of the plasma parameters in front of and normal to the anode surface, losses in axial direction may be substantially larger than in radial direction.

Conservation of charge carriers demands ion production in the anode fall which, however, amounts to only a small fraction (approximately 1 percent) of the total current.

Charge carrier generation in the anode fall zone may occur by two basically different ionization mechanisms, namely field ionization (F-ionization) and thermal ionization (T-ionization). Details of these processes are described by Bez and Höcker (21-26) and by Ecker (27).

Field ionization seems to play an important role in low intensity arcs where anode falls in the order of the ionization potential of the working fluid have been observed. For high intensity arcs which are of interest in the context of this paper, the anode falls are substantially lower (a few volts or even negative, depending on the anode geometry). For such arcs thermal ionization is the governing ionization mechanism. Electrons in the high energy tail of the Maxwellian distribution are responsible for ionization.

Previous anode fall theories (22-26) do obviously not apply to high intensity arcs with metallic anodes, because predicted anode falls (25) are substantially higher than those measured by various authors (28-32) even if uncertainties up to 100% are allowed for these measurements. Therefore, an attempt has been made to develop an anode fall theory which should apply to such arcs (33). Only the basic features of the model which has been adopted for this analysis will be discussed in this review in conjunction with some relevant results. Details of the model and the derivation and solution method of the governing set of equations are given in a thesis (33). In addition, a paper describing these details is in preparation.

2.3.1. BASIC FEATURES OF THE MODEL

Based on observations of the anode arc attachment in the CJD or AJD mode, it appears reasonable to employ a one-dimensional model for the anode boundary layer because the thickness of the anode boundary layer is substantially less than the diameter of the arc root. In addition, constant current densities are postulated within the anode boundary layer (channel model) as a first approximation. Inspection of the current density profiles calculated for the flow-effected zone (Figs. 12 and 13) indicate that this is indeed a valid approximation for the center part of the arc.

The temperature of the heavy species must drop across the anode boundary layer from values in excess of 10^4 K to typical anode temperatures ($< 10^3$ K). Since the electrical conductivity is almost zero at this temperature, electrons and heavy particle temperatures must separate in the anode boundary layer, i.e. the electron temperature should be substantially higher than the heavy particle temperature in order to meet the requirement of current continuity. This also implies that the usual conservation equations will no longer apply. For this reason, the conservation equations have been modified so that they account for the two-temperature situation in the anode boundary layer. In addition, the transport properties computed for this situation are utilized for solving the two-temperature conservation equations.

By specifying suitable boundary conditions at the anode as well as at the interface of the anode boundary layer and the flow-effected zone (some of these boundary conditions are based on experimental findings), the conservation equations have been solved for an atmospheric pressure argon arc assuming a range of current densities from 600 to 3,000 A/cm^2. Some representative results are shown in the following paragraph.

2.3.2. RESULTS

For the range of current densities covered by this analysis, the electron temperature departs strongly from the heavy particle temperature, in particular close to the anode. Fig. 18 shows a typical temperature distribution for an intermediate current density of

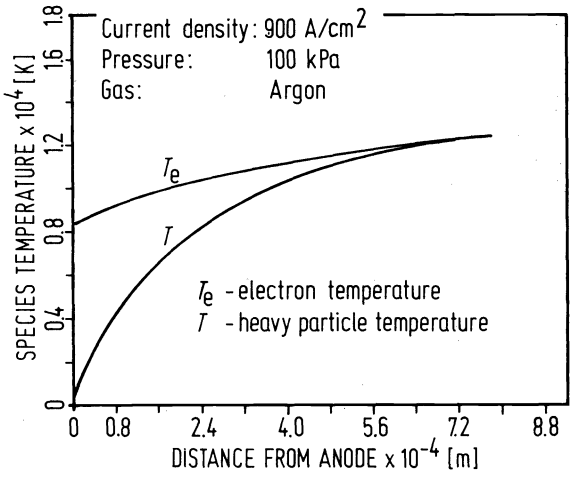

Fig 18 Typical distributions of electron and heavy particle temperatures in the anode boundary layer.

900 A/cm^2. Close to the anode, the heavy particle temperature approaches the temperature of the anode surface. The anode surface temperature which is one of the specified boundary conditions may range from 300 K up to the melting point of the anode material. The calculated temperature distribution, however, is not sensitive to variations of the anode surface temperature.

The electron temperature in the immediate vicinity of the anode surface shows relatively little variation for the entire range of current densities (8,000<T_e<10,000 K). Since the electrical conductivity is primarily a function of the electron temperature, the relatively high electron temperatures provide a sufficiently high electrical conductivity which is required for current continuity.

The thickness of the anode boundary layer depends on the current density as shown in Table I.

Table I: Thickness L of the anode boundary layer as a function of current density j

j (A/cm^2)	L (mm)
600	0.53
900	0.34
1,000	0.32
2,000	0.20
3,000	0.12

The edge of the anode boundary layer, on which the data in this table are based, is defined rather arbitrarily as the location at which $T_e - T = 0.1\ T_e$.

For the five cases listed in Table I the electric field has negative values over almost the entire thickness of the anode boundary layer. Fig. 19 shows a characteristic field strength distribution for a current density of 900 A/cm^2.

The electrons diffusing towards the anode are retarded by this field. The strong gradients of temperature and electron density which represent the driving forces for electron diffusion towards the anode overbalance the effect of decreasing electrical conductivity in

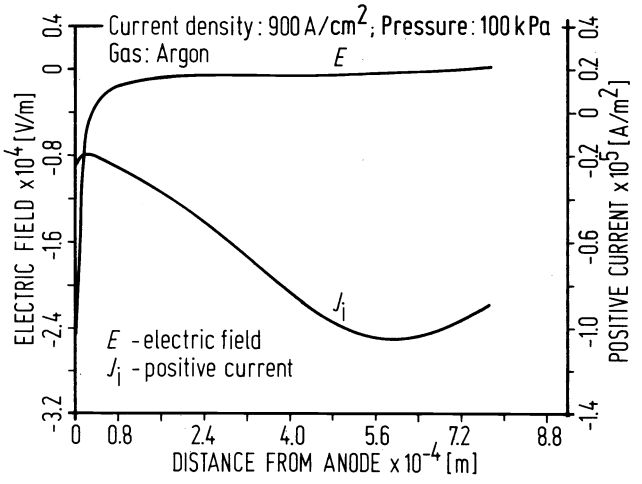

Fig 19 Field strength and ion current density in the anode boundary layer.

the vicinity of the anode. Therefore, the electron diffusion must be diminished by an opposing electric field to meet the requirement of current continuity.

In contrast to the results of previous investigations which predict strong positive fields in front of the anode and corresponding positive anode falls, the results of this work indicate negative anode falls for the range of current densities covered by this analysis. It is felt that this result will have important consequences for the design of high intensity arc devices including arc furnaces.

A modification of these results may be necessary in the case of sharply reduced anode surfaces (pointed anodes, for example). In this situation the electric field strength may reverse its sign due to the necessity of electron collection and the corresponding anode fall would then be positive. This situation requires at least a two-dimensional analysis.

The field strength shows a very steep slope in front of the anode (Fig. 19) indicating the presence of the sheath. The thickness of the sheath is by far too small to be discernible in this graph. The sheath is introduced as a boundary condition in the analysis as mentioned previously.

The negative field strength extending over the major part of the anode boundary layer is a consequence of the net positive space charge (Poisson equation) which forms in the vicinity of the anode. As indicated in Fig. 19, an ion current is induced by the electric field flowing towards the anode within the anode boundary layer. This ion current flow is responsible for the previously mentioned space charge. Since the anode is assumed to be catalytic, all ions arriving at the anode will be neutralized. The magnitude of the ion current density is in the order of 1% of the electron current density.

For calculating the potential drop across the sheath, the equation of random current density may be used, i.e.

$$j_r = \frac{e n_e \overline{v_e}}{4} \exp\left(\frac{e\phi_o}{kT_e}\right) \tag{8}$$

where ϕ_o is the potential drop across the sheath ($\phi_o<0$), and $\overline{v_e}$ the average thermal speed of the electrons. Since the contribution of the ions to the total current flow is negligible, current continuity requires that

$$j_r = j = \frac{e n_e \overline{v_e}}{4} \exp\left(\frac{e\phi_o}{kT_e}\right) \tag{9}$$

or $$\phi_o = - \frac{kT_e}{e} \ln \left(\frac{en_e\overline{v_e}}{4j} \right) \quad (10)$$

By using Eq. (10) the potential drop across the sheath has been calculated. The results are summarized in Table II.

Table II: Potential drop ϕ_o across the sheath as a function of the current density.

$j(A/cm^2)$	$\phi_o(V)$
600	- 2.2
900	- 1.8
1,000	- 1.9
2,000	- 1.5
3,000	- 2.7

The total potential drop across the anode boundary layer is almost identical with ϕ_o because the integration of the electric field over the thickness of the anode boundary yields only a small correction term. Although the parameter which has the strongest effect on ϕ_o is the current density, the plasma temperature at the outer edge of the anode boundary layer also affects ϕ_o.

3. HEAT TRANSFER TO THE ANODE

In the previous sections the behavior and the properties of the various layers have been discussed which comprise the anode region of a high intensity arc (Fig. 1). It has been already demonstrated that the energy transport mechanisms in the flow-effected zone have a strong influence on anode heat transfer. As will be shown in this section, anode heat transfer is also affected by the properties of the anode boundary layer, including the sheath.

In the first part of this section, the conventional anode heat transfer model will be discussed as well as a new model which is based on the two-temperature anode boundary layer description. The second part deals with critical anode heat fluxes which cause either melting or evaporation of the anode material. Finally, in the last part of this section, some recent experimental work will be reviewed associated with local heat transfer measurements and the effect of the cathode jet on anode heat transfer.

3.1 ANODE HEAT TRANSFER MODELS

According to the conventional heat transfer model based on positive anode falls, local heat fluxes to the anode may be expressed by (34):

$$q_a = q_c + q_r + j_e\left(\frac{5}{2} \frac{kT_e}{e} + V_a + \phi_a \right) \quad (11)$$

In Eq. (11), q_c represents local heat fluxes by conduction and convection, q_r represents the radiative heat flux from the arc which is absorbed by the anode, and the last term represents the energy transferred by the electrons to the anode. T_e is the temperature of the electrons entering the anode fall zone, ϕ_a is the work function of the anode material,

V_a is the anode fall, and j_e is the electron current density. The first term in parenthesis represents the electron enthalpy neglecting the effects of axial gradients of electron density and electron temperature. The sheath which is assumed to be identical with the positive anode fall is treated as collisionless. It should be pointed out that this model applies only if the previously mentioned assumptions hold; in particular it holds only for arcs with positive anode falls.

For the two-temperature anode boundary layer the anode heat transfer model assumes the form

$$q_a = q_{conv} + q_r - k_e \frac{dT_e}{dx} - k_a \frac{dT}{dx} + j \left(3.2 \frac{kT_e}{e} + \phi_a\right) \tag{12}$$

where q_{conv} represents convective and q_r radiative heat transfer. The following two terms account for heat conduction to the anode by the electrons and the heavy particles, respectively. The first term in parenthesis has now a factor of 3.2 instead of 2.5 attached. This change accounts for axial gradients of electron temperature and density (33). The current density in Eq. (12) contains besides the usual electric field contribution, two more terms, i.e.

$$j = \sigma \left(E + \frac{1}{en_e} \frac{dp_e}{dx}\right) + \phi \frac{dT_e}{dx} \tag{13}$$

In this equation σ represents the electrical conductivity, E the field strength, p_e the partial pressure of the electron gas, and ϕ the thermal diffusion coefficient.

It should be noticed that Eq. (12) does not contain the anode fall which is negative in this case. If the anode fall is positive, then the electrons will be accelerated across the sheath and they transfer the energy gained in this process to the anode. Depending on the magnitude of the electric field strength, the electron distribution function may be severely distorted in this case. In contrast, the electrons approaching an anode with a negative anode fall retain their Maxwell-Boltzmann distribution corresponding to the prevailing electron temperature. The negative field strength, however, will reduce the number of electrons reaching the anode surface, but it will not affect their energy. Therefore, it would be wrong to use Eq. (11) with a negative value of V_a. This finding should have important consequences for the interpretation of experimental anode heat transfer data and, even more important, for the design of arc plasma equipment.

3.2 CRITICAL ANODE HEAT FLUXES CAUSING MELTING OR EVAPORATION

Since high intensity arcs are frequently constricted in front of the anode, the specific heat fluxes may exceed the capabilities of water cooling, i.e. melting of the anode surface or, in the worst case, burn-out will occur at the location of the highest specific heat flux. In this paragraph the results of recent calculations (35) will be summarized considering the critical steady-state heat fluxes which cause either melting or evaporation on anode surfaces.

The main assumptions used for modeling this situation are listed below:

1) The arc subjects the anode to a constant, uniform heat flux, q_a, over a circular attachment region of radius R.

2) The problem possesses axisymmetry.

3) The water-cooled rear face of the anode is at a constant temperature T_w.

4) The anode radius is very large compared to its thickness ($R \to \infty$) so that for $R \to \infty$ the steady-state temperature will be very close to the temperature of the water cooled rear face, and the conduction heat flux in radial direction is negligible.

5) The radiative heat loss from the front face of the anode is described by $q_{re} = \varepsilon\sigma T_s^4$ where T_s is the local temperature of the front face.

6) In cases where melting occurs, the melt zone is free of any kind of convective currents.

7) Heat losses and mass losses due to ablation and evaporation of the anode material are negligible.

8) Ohmic heating of the anode is negligible.

Although the "channel model" defined by the first assumption appears to be a rather crude approximation, the heat flux distributions discussed in part 2.2 indicate that this is indeed a reasonable approximation.

The third assumption is somewhat arbitrary. What is implied here is that the heat transfer coefficient between the rear face of the anode and the cooling water is very large and hence the anode surface temperature is approximately equal to the cooling water temperature (400 K). Assumption of a specific value for the heat transfer coefficient would be equally arbitrary. A combined analysis of the water-cooling and anode conduction process would certainly be more accurate; but it would also be considerably more complicated and involve a commitment to a particular cooling water flow configuration.

In many practical applications, thin, disk-shaped anodes are used, which makes assumption (4) reasonable. The fifth assumption implies that none of the energy radiated by the front face of the anode is reflected or reradiated back to it; this allows a maximum radiation loss from the front face. The analysis shows that even with this assumption, the total radiation heat loss from the front face is a very small fraction of the total heat transfer from the arc to the anode. Hence no significant error is involved in assumption (5). In cases where melting of the anode material occurs, the melt zones are usually very thin and hence, even with the very large temperature gradients that exist in these zones, it is expected that no bouyancy driven convection currents are established in them. The possibility of surface tension driven convection currents (Marangoni effect) has not been investigated. For some orientations of the anode, the melt zone could flow under the action of gravity; however, this possibility has not been considered in this analysis. Surface tension would prevent such flows in the case of very thin melt layers. Otherwise, this model is strictly valid only in the case where the anode is horizontal and the arc attaches to the upper surface. Heat and mass losses due to evaporation of the melt zone may not be negligible in all cases, especially in the central portions of the attachment region, when the surface temperatures are close to the boiling temperature of the anode material. However, for the sake of simplicity, this effect has not been included in this analysis. Inclusion of a simple model for evaporation from the front face of the anode is not a difficult task in itself, but experimental data on the constants appearing in Fick's Law or Arrhenius' Law are not readily available in the literature for common anode materials like tungsten and copper. The assumption of negligible Ohmic heating is valid for the current range covered by this analysis.

The two-dimensional steady-state heat conduction equation has been solved numerically with appropriate boundary conditions. These boundary conditions as well as the solution method are described in Ref. (35). The variation of the critical heat fluxes with respect to melting and boiling as a function of the radius, R, of the arc attachment zone, have been obtained for two typical anode materials, copper and tungsten (for 1 mm$\leq$R$\leq$10 mm; L = 2 mm and L = 2.5 mm). The results for copper are presented in Fig. 20 and those for tungsten in Fig. 21. The upper curves correspond to $q_{crit,\ boiling}$ and the lower ones represent $q_{crit,\ melting}$.

It is evident from Figs. 20 and 21 that the critical heat fluxes drop sharply with increasing R in the range, 1 mm$\leq$R$\leq$3 mm, and more gradually in the range, 3 mm$\leq$R$\leq$10 mm. Both $q_{crit,\ melting}$ and $q_{crit,\ boiling}$ approach asymptotically constant lower bounds. For large values of R, the heat transfer process becomes almost one-dimensional, leading asymptotically to a lower bound for q_{crit}. In contrast, for small values of R the heat conduction process is two-dimensional and the required heat flux for melting or evaporation becomes substantially larger because of the high heat losses. This fact has interesting consequences as far as the anode attachment is concerned. Relatively small attachment areas are better cooled, i.e. they can tolerate larger local heat fluxes without overheating. Therefore, if the anode root can be split into several spots (multiple anodes) erosion problems may be less severe.

The boiling and melting temperatures of tungsten are higher than those of copper, and this might lead one to suspect that the critical heat fluxes for tungsten would also be higher than those for copper. However, an examination of Fig. 20 and 21 reveals that the critical heat fluxes for tungsten, for most of the R values considered, are somewhat lower than those for copper. This is so because the thermal conductivity of tungsten is about

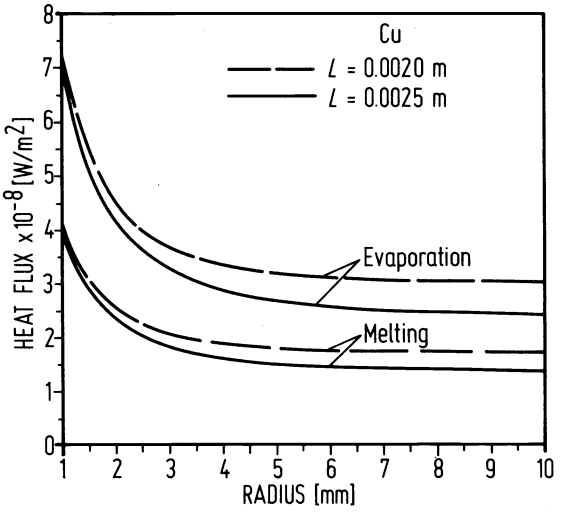

Fig 20 Critical heat fluxes for copper anodes.

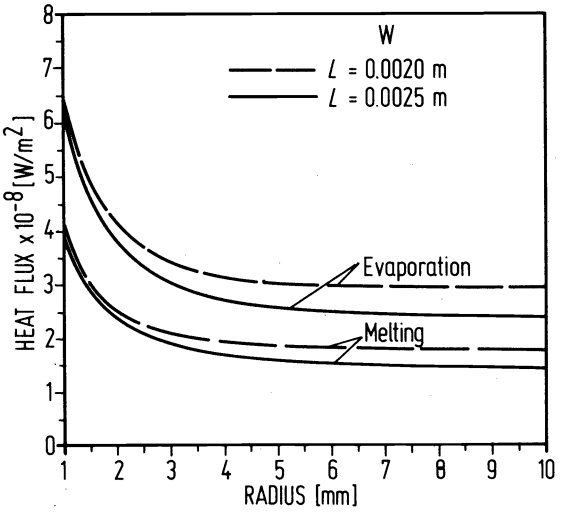

Fig 21 Critical heat fluxes for tungsten anodes.

one-third of that of copper. Hence, for the same temperature gradient, copper can be expected to conduct about three times as much heat as tungsten. The melting and boiling temperatures of tungsten are 2.7 times and 2.1 times higher than the corresponding temperatures for copper.

In all computations it was observed that $q_{re} \sim 10^5$ W/m^2. In contrast, $q_{crit,\ melting} \sim 10^8$ W/m^2, and $q_{crit,\ boiling}$ values are even higher. Hence radiation heat losses from the front face of the anode do not have a significant influence on the critical heat flux values.

In the following, the critical heat fluxes as shown in Figs. 20 and 21 will be compared with heat fluxes derived form Eq. (12). The use of this equation implies that the anode fall is negative. Fortunately, a number of simplifications can be applied to Eq. (12). The analysis described in part 2.2 demonstrates that the last term in Eq. (12) is by far more important than the other terms in this equation. Therefore, the following approximation will be used for this comparison:

$$q_a \simeq j \left(3.2 \frac{kT_e}{e} + \phi_a\right) \qquad (14)$$

Table III: Comparison of calculated critical heat fluxes with those derived from (36) ($L = 2.5$ mm, $T_w = 400$ K).

Current; mass flow rate in 10^{-5} kg/s	gas	anode material	Radius of arc attachment (mm)	q_a in $10^8 W/m^2$	$q_{crit, melt}$ in $10^8 W/m^2$	$q_{crit, boil}$ in $10^8 W/m^2$
I = 500 A		Cu	3.4	2.7	1.7	3.1
$\dot{m} = 4.7$	N_2	W	3.4	3.1	1.75	2.8
I = 500 A		Cu	3.8	2.0	1.65	2.9
$\dot{m} = 3.2$	N_2	W	3.8	2.1	1.70	2.7
I = 500 A		Cu	4.2	1.4	1.6	2.85
$\dot{m} = 3.3$	Ar	W	4.2	1.5	1.65	2.65
I = 500 A		Cu	3.1	2.8	1.8	3.2
$\dot{m} = 6.3$	Ar	W	3.1	2.9	1.85	2.95

The work function ϕ_a for Cu is taken as 3.9 V and for W as 4.5 V. More problematic are reliable values of j and T_e. Liu (36) calculated current densities and temperatures in the anode region of atmospheric pressure nitrogen and argon arcs assuming LTE. As shown in Fig. 18, the electron temperature changes relatively little across the anode boundary layer. Therefore, in a first approximation, the LTE temperatures calculated by Liu (36) outside the anode boundary layer will be identified with the electron temperature close to the anode. The current density j will be taken as the maximum current density also calculated in (36). Values of q_a derived from (36) in this way are listed in Table III. The values of q_{crit} (melting and evaporation) are also listed for comparison, based on $T_w = 400$ K and $L = 2.5$ mm. The radius of the anode arc attachment with the associated mass flow rate at a given current of 500 A is also taken from (36).

Arcs in nitrogen which tend to be more constricted at the anode than arcs in argon at comparable induced mass flow rates, consistently reveal heat fluxes exceeding those required for melting. In fact, in some cases the anode heat fluxes approach or even exceed those required for evaporation, indicating that some anode vapor will be present, a finding which has been confirmed by corresponding experiments. In the case of argon arcs, the anode heat fluxes are below those required for melting, unless the induced flow is allowed to increase so that the resulting anode attachment area shrinks substantially. Table III also reveals that there is no advantage of using an electrode material with substantially higher melting and boiling points (W). The advantage of the delayed phase change is offset by the lower thermal conductivity and the higher work function, ϕ_a, of W compared with Cu.

3.3 MEASUREMENT OF HEAT FLUXES IN PULSED HIGH-CURRENT ARCS

Pulsed high intensity arcs with currents around 5 kA have been used for determining anode heat fluxes in the center part of the anode arc root. The method for measuring such heat fluxes is based on a comparison of measured temperature histories of the rear face of very thin anodes with calculated temperature histories assuming certain heat fluxes into the front face of the anode. In addition, high speed streak photographs of the arc taken close to the anode provide the necessary timing information needed for the development of a

suitable model. This is particularly important for the initial, transient phase of the arc.

The total duration of a current pulse is 200 μs. Since a lumped-parameter network is used as a power source, the current reaches a constant plateau after 10 μs and after approximately 100 μs the arc becomes quasi-steady. Heat fluxes measured in this regime apply also to steady arcs operated under otherwise identical conditions.

Details of the method are described in Ref. (37). Results for the quasi-steady part of a 5 kA pulsed arc in argon and nitrogen atmosphere using different anode materials reveal heat fluxes of approximately 25 kW/cm^2 for argon and up to 100 kW/cm^2 for nitrogen arcs (38). The anode material is not a parameter as long as melting and evaporation of the surface is avoided. The cathode conditions (thoriated tungsten with a 60° conical tip) have a strong effect on anode heat transfer. Since the electrode gap is only 10 mm, the cathode jet will impinge on the anode surface. As shown in (15), a slight rounding of the cathode tip has a significant effect on the cathode jet velocity. Therefore, convective heat transfer to the anode will be substantially reduced with "seasoned" cathodes. The data in Ref. (38) also show that convective heat transfer plays an important role in this particular arrangement. In fact, the reduction of the total anode heat transfer by 50% in some of the experiments with "seasoned" cathodes indicates that convective heat transfer may be the dominant heat transfer mechanism at this high current level. Measurements in steady-state free-burning arcs at current levels in excess of 1 kA corroborate this result (39).

Investigations of the initial phase of a pulsed 6 kA arc in argon at 1 atmosphere show that the arc initially attaches to the anode in the form of a current-carrying shell (40). This fact is explained by the fast rise of the current pulse and the resulting skin effect. As the cathode jet forms, the current distribution rearranges and reaches after approximately 100 μs a quasi-steady state with the peak current density presumably in the center. Heat fluxes at the anode axis are very low during the 10 to 15 μs shell attachment period. The heat flux rises to a peak value of 2×10^9 W/m^2 after steady state current is reached. The high heat flux plateau declines to the quasi-steady state heat flux as the expanding cathode jet increases the anode attachment area and the current density decreases in the center. Heat fluxes of 9×10^7 to 1.5×10^8 W/m^2 are measured after stabilization of the stagnation flow regime results in quasi-steady state operation of the arc. Again, the importance of the cathode jet on anode heat transfer is obvious for this initial phase of an arc. The maximum heat flux of 2×10^9 W/m^2 which seems to coincide with the arrival of the cathode jet on the anode surface is, however, only partially due to convection. At this time it appears that concentration of the arc current within the relatively small cross section of the cathode jet is primarily responsible for the peak in the heat flux distribution.

4. ACKNOWLEDGEMENTS

Most of the work reported in this survey has been supported by the National Science Foundation, grant numbers ENG 71-02478 and ENG 77-04108.

REFERENCES

1. R. G. Gold, W. R. Sandell, P. G. Cheplick and D. R. Mac Rae, Proceedings of the Internatl Symp. on Metal-Slag-Gas Reactions and Processes, Toronto, 1975; Electrochemical Society, 969 (1975).
2. D. R. Mac Rae, R. G. Gold, C. D. Thompson and W. R. Sandell, 34th Electric Furnace Conf., St. Louis, Mo. (1976).
3. M. I. Boulos and W. H. Gauvin, The Canadian J. of Chem. Eng. 52, 355 (1974).
4. P. A. Wilks, private communication
5. O. Matsumoto, H. Hirose, Y. Kawara, and T. Ohue, High Temp. Sci. 9, 27 (1977).
6. I. G. Sayce, Adv. Ext. Met. Refining Proc. Int. Symp. 241 (1971).
7. N. N. Rykalin, 2nd Internatl. Symp. on Plasma Chemistry, Roma/Italy (1975).
8. S. M. L. Hamblyn, A Review of Application of Plasma Technology with Particular Reference to Ferro-Alloy Production, Rep. No. 1895 Nat. Institute for Metallurgy, Randburg, South Africa (1977).
9. P. Fauchais and E. Bourdin, Third Internatl Symposium on Plasma Chemistry, University of Limoges/France (1977).
10. G. Perugini, High Temperature Physical Chemistry Applied to Plasma Synthesis and Surface Phenomena on Special Ceramics, Rep. of the G. Donegani Research Institute/ Montedison, Novara, Italy (1977).
11. C. Bonet, CEP 63, (1976).

12. E. Pfender, Pure & Appl. Chem 48, 199 (1976).
13. H. Maecker, Z. Physik 141, 198 (1955).
14. N. A. Sanders, The Effect of Anode Evaporation on the Behavior of a High Intensity Arc, Master Thesis, Univ. of Minnesota, March 1979.
15. T. W. Petrie and E. Pfender, Welding J., Research Supplement 49, 588-s (1970).
16. W. Finkelnburg and H. Maecker, Electric Arcs and Thermal Plasmas, Handbook of Physics 22, 254 (1956), Springer-Verlag, Germany.
17. T. S. Chou and E. Pfender, Wärme-und-Stoffübertragung, Bd. 6, No. 2, 69 (1973).
18. E. Pfender and J. Schafer, J. Heat Transfer 97, Ser. C, No. 1, 41 (1975).
19. C. H. Liu and E. Pfender, Heat Transfer in the Anode Region of High Intensity Arcs, Eckert-Festschrift, Hemisphere Publishing Co. (1979).
20. C. H. Liu, Numerical Analysis of the Anode Region of High Intensity Arcs, Ph. D. Thesis, Univ. of Minnesota (1977).
21. W. Bez and K. H. Hoecker, Z. Naturforsch. 9a, 64 (1954).
22. W. Bez and K. H. Hoecker, Z. Naturforsch. 9a, 72 (1954).
23. W. Bez and K. H. Hoecker, Z. Naturforsch. 10a, 706 (1955).
24. W. Bez and K. H. Hoecker, Z. Naturforsch. 10a, 714 (1955).
25. W. Bez and K. H. Hoecker, Z. Naturforsch. 11a, 118 (1956).
26. W. Bez and K. H. Hoecker, Z. Naturforsch. 11a, 192 (1956).
27. G. Ecker, Ergebnisse d. exakt. Naturwiss. 33, 1 (1961).
28. T. K. Bose and E. Pfender, AIAA Journal 8, 1643 (1969).
29. G. Busz-Peuckert and W. Finkelnburg, Z. Phys., Bd. 140, 540 (1955).
30. P. Schoeck and F. Maisenhälder, Beiträge aus der Plasmaphysik, Heft 5, 345 (1966).
31. M. Sugawara, Brit. J. Appl. Phys. 18, 1777 (1967).
32. I. G. Kesaev, Soviet Phys. Tech. Phys. 9, 1146 (1965).
33. H. Dinulescu, Analysis of the Anode Boundary Layer of a High Pressure-High Current Arc, Ph. D. Thesis, Univ. of Minnesota (1979).
34. E. R. G. Eckert, And E. Pfender, Advances in Plasma Heat Transfer, Advances in Heat Transfer 4, Academic Press, New York, (1967).
35. B. R. Baliga, C. H. Liu, and E. Pfender, ASME 78-HT-10 (1978).
36. C. H. Liu, Numerical Analysis of the Anode Region of High Intensity Arcs, Ph. D. Thesis, University of Minnesota, (1977).
37. J. L. Smith and E. Pfender, Rev. Sci. Instrum. 47, No. 9, 1056 (1976).
38. J. L. Smith and E. Pfender, IEEE Transactions on Power Apparatus and Systems PAS-95, No. 2, 704 (1976).
39. R. C. Eberhart and R. A. Seban, Internat. J. Heat Mass Transfer 9, 939 (1966).
40. D. Johnson and E. Pfender, IEEE Transact. Plasma Science, PS-7 No. 1, 44 (1979).